Available online at www.sciencedirect.com
SCIENCE DIRECT®
Energy 30 (2005) 427–445
ENERGY
www.elsevier.com/locate/energy

A KIVA code with Reynolds-stress model for engine flow simulation

S.L. Yang [a,*], Y.K. Siow [a], C.Y. Teo [a], K. Hanjalic [b]

[a] *Mechanical Engineering-Engineering Mechanics Department, Michigan Technological University, Houghton, MI 49931, USA*

[b] *Department of Applied Physics, Thermofluids Section, Delft University of Technology, Lorentzweg 1, 2628 CJ Delft, The Netherlands*

Abstract

To properly simulate the highly anisotropic turbulent engine flows, higher order turbulence model should be used to correctly reproduce flow physics inside the engine. The popular KIVA computer code has been modified to include the Reynolds-stress turbulence model (RSTM) for this purpose. The objective of this paper is to present our recent research on the use of RSTM and the KIVA code for engine flow simulation, which include gas turbine combustors and IC engines.

1. Introduction

Fluid flows in engines are always turbulent and are highly anisotropic due to complex geometry, wall effects, flow rotation (swirl), internal separation, etc. For internal combustion (IC) engine flow, additional complications are involved because of the rapid compression and expansion strokes produced by the piston motion. Among these flow phenomena, swirl is an essential and desirable engine design feature. Modern gas turbine combustors use strong swirl to improve combustor performance by aiding in the fuel–air mixing process and by producing recirculation regions which can act as flame holders for flame stability [1]. For direct-injection IC engines, swirl is used to enhance the air–fuel mixing for emission control and better efficiency. Therefore, to properly simulate flow field inside various types of engines, the swirl characteristic needs to be resolved by a robust and versatile turbulence model, without having to perform ad hoc modifications for each engine geometry.

* Corresponding author. Fax: +1-906-487-2822.
E-mail address: slyang@mtu.edu (S.L. Yang).

0360-5442/$ - see front matter © 2004 Elsevier Ltd. All rights reserved.
doi:10.1016/j.energy.2004.09.004

Most industrial computations of engine flows are performed using two equation models, such as the κ–ε or the κ–ω model, in which the Boussinesq approximation is used to relate the Reynolds stress tensor ($\overline{u_i u_j}$) to the mean flow strain rate (S_{ij}), i.e.,

$$\overline{u_i u_j} \propto S_{ij} \tag{1}$$

The proportionality coefficient, the eddy viscosity (μ_t), in the κ–ε model is expressed in terms of fluid mean density ($\bar{\rho}$), turbulence kinetic energy (κ), and its dissipation rate (ε)

$$\mu_t \propto \frac{\bar{\rho}\kappa^2}{\varepsilon} \tag{2}$$

Since $\bar{\rho}$, κ, and ε are all scalars, accordingly, the eddy viscosity is isotropic in contrast to real situation in complex flows. The Reynolds-stress (second-moment) turbulence model (RSTM), on the other hand, does not suffer from this shortcoming.

Within the framework of the Reynolds averaging approach, the RSTM represents the most comprehensive description of turbulent flows, and can be employed for practical computations with the present-generation workstations [2]. One major advantage of RSTM is that the source terms are exact and need not be modeled. This becomes especially important in flows with complex strain field where in addition to simple shear, dilation and compression strain are significant [2]. Since each Reynolds-stress component is described by a transport equation, the RSTM *naturally* includes effects of anisotropy, streamline curvature, sudden changes in strain rate, secondary motions, flow rotation.

Two RSTMs, namely the LRR [3] and the SSG [4] models, were implemented into the popular KIVA [5] family computer codes. The LRR model, especially its IP version, is often referred to as the standard RSTM, characterized by the simple linear models of the pressure–strain redistribution process, but for the near-wall flows, it requires the inclusion of a wall-reflection term (not accounted for here). The SSG model is considered a quasi-linear model since it contains one quadratic term in the pressure–strain model. One advantage of using the SSG model is that, unlike most other RSTMs available in the literature, no wall-distance parameter for accounting for wall-reflection term is needed. This is a desirable feature for reciprocating engine flow simulations, since the computational domain is of a complex shape and changes constantly in time due to piston motion.

The objective of this paper is to present recent studies by the authors on the use of the RSTM and KIVA code for engine flow simulation. The results to be presented include (1) multi-point lean direct injection (LDI) gas turbine combustor with discrete jet swirlers, (2) multi-point LDI gas turbine combustor with helical axial swirlers, (3) a simplified direct injection stratified charged (DISC) IC engine, (4) a lean-premixed prevaporized (LPP) combustor, and (5) a four-valve double overhead camshaft (DOHC) IC engine. Due to space limitation, the Reynolds-stress modeling equations, details of the KIVA code implementation, and code validation will not be presented here, but can be found in Yang et al. [6].

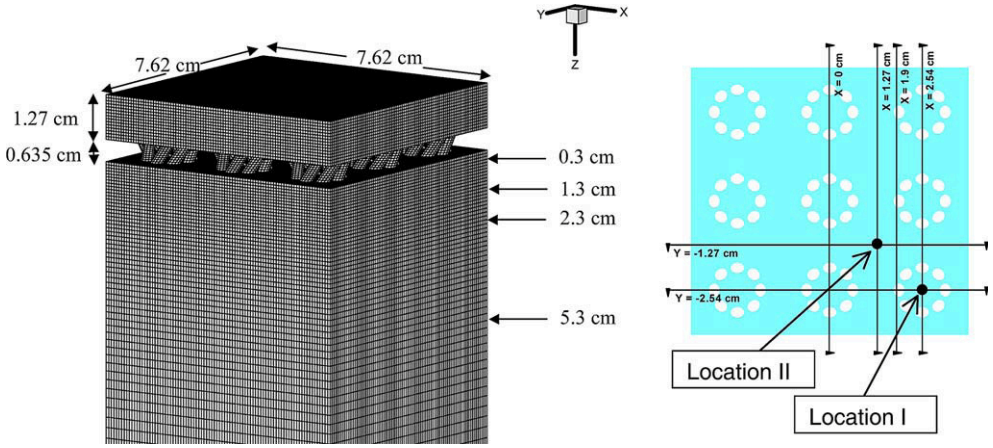

Fig. 1. Computational grid of the entire domain, dimensions, and the cutting plane locations.

2. Results and discussion

2.1. LDI combustor with discrete jet swirlers

The multi-point LDI combustor has a rectangular inlet section 12.7 mm long (Fig. 1), and is upstream of nine groups of swirlers arranged in a 3×3 pattern (Fig. 2). Each group of swirlers comprises eight passages, all co-rotated at 35° in the tangential direction (Fig. 3). A 177.8 or 76.2 mm-long rectangular burner duct is downstream of the swirler section. The combustor has a cross section of 76.2 mm $\times$ 76.2 mm. The inlet surface of the combustor lies in the X–Y plane and the inlet velocity is specified to be in the axial or positive Z direction. The final Cartesian computational mesh shown in Fig. 1 has a total of 965,905 cells and 967,312 vertices.

For comparison, the primary flow conditions were identical to the parameters in a report by Iannetti et al. [7] in which the NASA National Combustor Code (NCC) [8] was used along with a cubic nonlinear κ–ε model tuned for swirl flow calculation [9]. The inlet axial velocity was

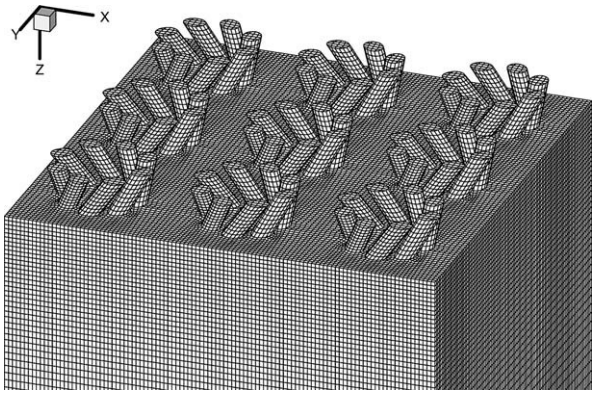

Fig. 2. Discrete jet swirlers in 3×3 pattern atop the burner duct.

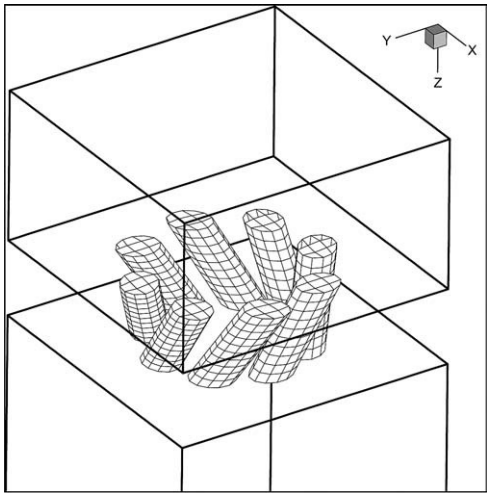

Fig. 3. Computational grid of a single discrete jet swirler.

6.6 m/s. Law-of-wall was applied on all solid walls. In addition, the turbulence intensity and length scale were assumed 10% and 3%, respectively, at the inlet. The exit temperature and pressure were at the ambient condition.

The primary goal of this study is to investigate the non-reacting flow field of a multi-point injector in a square duct, and to compare results of the SSG model with the cubic nonlinear κ–ε model in NCC and the LDV measurements from an experimental study. As the measurements were made in a non-reacting flow, only cold-flow calculations are presented. The LDV data are taken from a report by Jeng et al. [10] and the NCC results from Ref. [7]. In Ref. [7], tetrahedral grids were used with 2.26 million cells and 2.28 million vertices for a quarter domain of the combustor. Comparisons of results are presented in color contours, in both X–Y and Y–Z planes, i.e., at $Z = 3$, 13 and 23 mm, as well as $X = 19$ mm (between swirlers). These cutting plane locations are shown in Fig. 1.

In general, the results in the X–Y planes show that the RSTM yields a better agreement with the experiment than the NCC κ–ε calculations. At $Z = 3$ mm (Fig. 4), although the magnitude

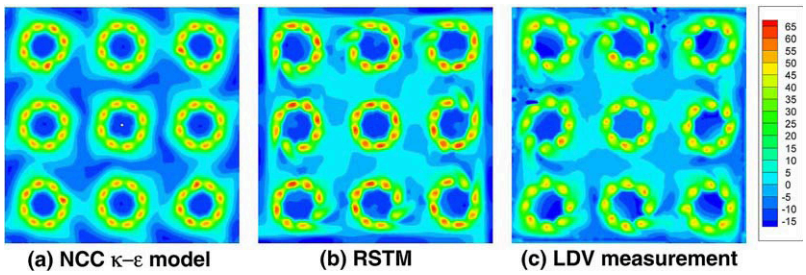

Fig. 4. Comparison of axial velocity among NCC κ–ε result, RSTM result, and LDV measurement at $Z = 3$ mm. (For interpretation of the references to color in these figures, the reader is referred to the web version of this article.)

of the forward velocity contours compares fairly well between the measured and both computed results, the NCC-calculated reverse-flow structures differ substantially. In Fig. 4a, the dark blue contours surrounding the center swirlers represent large areas of strong recirculation, which are not present in both Figs. 4b (RSTM) and c (LDV). The RSTM result, Fig. 4b, agrees quite well with the measurement, particularly the forward-flow regions directly below each swirler.

Further downstream, at $Z = 13$ mm (Fig. 5), the NCC computation shows circular recirculation zones below the center of the swirlers, where both the RSTM and the experimental measurements show kidney-shaped reverse-flow regions. In Ref. [7], it was assumed that the combustor geometry was rotationally periodic every 90°. While this is true in geometric terms, the LDV data in both Figs. 4 and 5 show that the flow field is not symmetrical about both the X- and Y-axes. This is caused by the flow-field structure induced by the interactions among the co-rotating swirlers. Therefore, a periodic boundary condition may not be appropriate for this geometry and swirler configuration.

The line plots in Figs. 6 and 7 show quantitative comparisons between the measurements and computations. Since in the LDV experiment two velocity components, U (cross-flow) and W (axial), were measured, it is appropriate to present comparisons in terms of these components. Fig. 6a contains line plots of U-velocity comparison among the measured and computed results, while Fig. 6b shows the W-velocity comparison.

Fig. 6a-I presents the U-velocity at axial locations downstream of the bottom, right swirler (location I in Fig. 1). Observing the LDV data, its trend shows an axial shift of momentum from the presence of neighboring swirlers. Such behavior is successfully captured by the RSTM, while the NCC κ–ε model, unable to resolve the peak, computed much lower values, particularly before $Z = 3.0$ cm where recirculation is strong. Fig. 6a-II contains a line-plot comparison of the U-velocity along axial locations between the four bottom-right swirlers (location II in Fig. 1). The RSTM shows a close agreement with the LDV data, with a maximum offset near $Z = 1.0$ cm.

Figs. 6b-I and II quantitatively present the axial velocity component (W), at the two locations as in Fig. 6a. In Fig. 6b-I, from the LDV data, zero axial-velocity occurs at approximately $Z = 2.2$ cm downstream of the swirler, which may be assumed to be the size of the recirculation

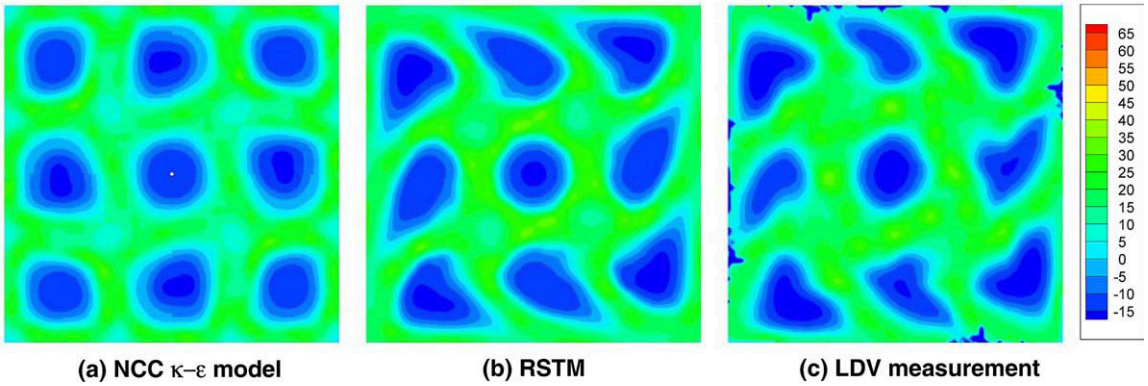

Fig. 5. Comparison of axial velocity among NCC κ–ε result, RSTM result, and LDV measurement at $Z = 13$ mm.

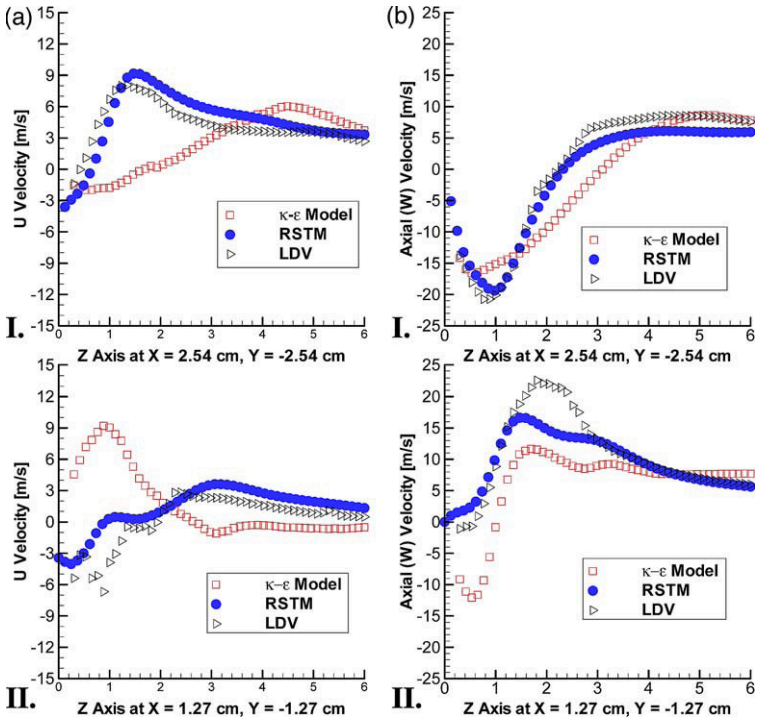

Fig. 6. Line plots of velocity components.

bubble. The RSTM profile closely follows the LDV data, although a maximum offset of 25% occurs below the recirculation region. The NCC's κ–ε model computed a bubble size nearly twice the measured one. Fig. 6b-II, on the other hand, does not show as distinct a comparison as does Fig. 6b-I. The RSTM result exhibits the general trend of the LDV profile for $Z <$ 1.0 cm as well as $Z > 3.0$ cm. The NCC calculates a substantially stronger reversed flow in the $Z < 1.0$ cm region.

Although the V-velocity component was not directly measured in the LDV experiment, it would still be useful to show the line plots of swirl velocity and turbulence kinetic energy, κ. The plots that follow, therefore, serve as comparisons of trend rather than accuracy. The swirl velocity in Fig. 7a-I carries a characteristic similar to the U-velocity plot in Fig. 6a-I. The swirl quickly peaks at about $Z = 1.4$ cm, then gradually settles. The RSTM basically follows the trend and stays within 20% of the measured values. The cubic non-linear κ–ε model was unable to resolve any swirl structure within the recirculation zone. Fig. 7a-II shows a more complex profile, particularly for $Z < 3.0$ cm. The measured swirl values are generally lower than those in Fig. 7a-I, and fluctuate considerably inside the bubble. The κ–ε model generally yields excessive swirl up to $Z = 2.5$ cm. Halfway downstream and onward, however, all computed results agree quite well with the LDV measurements.

Fig. 7b-I shows that the NCC's κ–ε model fails to capture the steep profile of the measurements, near $Z = 1.5$ cm. Instead, the model gives a generally flat line that falls below the LDV data. Since eddy viscosity, μ_t, is directly proportional to the square of κ, a small κ value

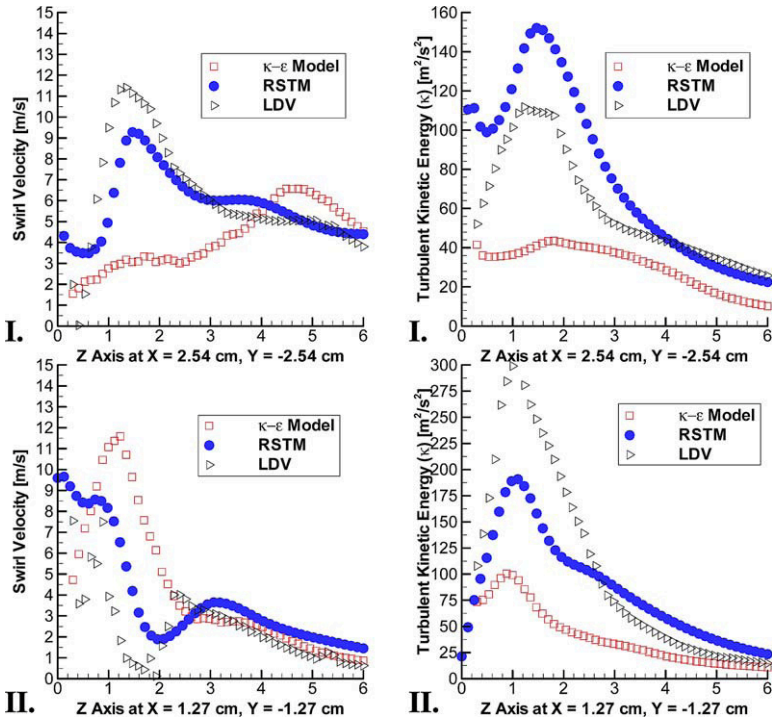

Fig. 7. Line plots of swirl velocity and turbulence kinetic energy.

results in an even smaller μ_t. In Fig. 7b-II, all calculated results fall below the LDV data while exhibiting similar trend.

Details of this study can be found in Ref. [11].

2.2. LDI combustor with helical axial swirlers

Configuration of this case is similar to the previous one, except that helical axial swirler is used. The modeled combustor includes nine axial swirlers with venturi, which are attached to a single primary combustion zone, Fig. 8. The helical axial swirlers are arranged in a 3×3 square and lies in the X–Y plane. The rotation imparted to the air by each swirler is directed in the axial or Z-direction. Two different swirlers are used based on blade angle inclination from the direction of airflow. One swirler has a 45° angle, and the other 60°. These angles refer to the outermost vane angle of the helical swirler. A plot of a 60° swirler attached to a convergent–divergent venturi is shown in Fig. 9. The central hollow region is reserved for the fuel injector while the five helical hollow slots represent the blades that guide the airflow.

The computational domain begins with the inlets placed at the top of nine 45° or 60° swirlers. These swirlers are co-rotating clockwise. After air exits, a swirler it passes through a venturi. A short divergent cone, acting like a diffuser, follows and ends at the primary zone inlet plane. One constant Y plane and two constant Z planes are defined for postprocessing, where Z represents the axial direction. These cutting plane locations are also shown in Fig. 8.

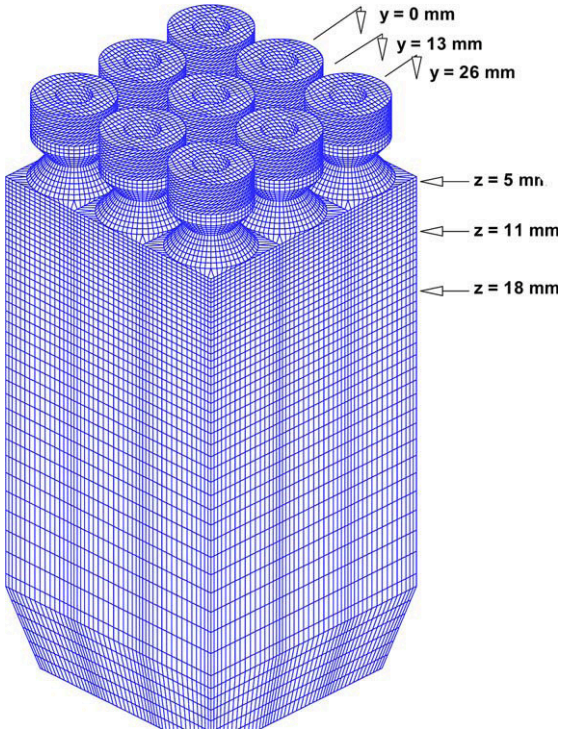

Fig. 8. Computational model and cutting planes.

Notable boundary conditions include the wall and inlet boundaries. Since the turbulence equations presented are valid only for high *Re* number flows, wall functions were used for wall

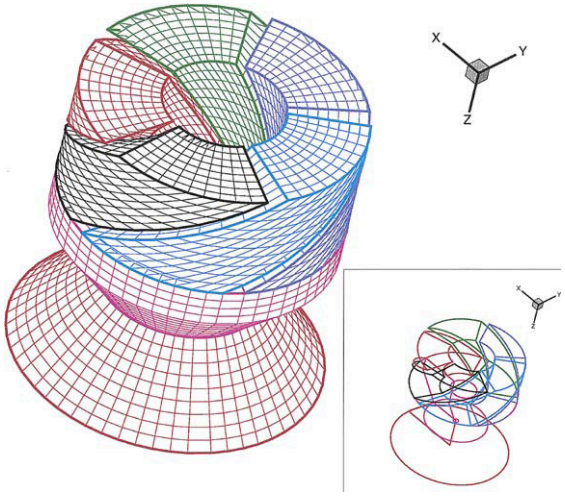

Fig. 9. A sketch of the axial swirler.

boundaries. Diffusion fluxes were set to zero at the walls. The specified inlet velocity value depends on the chosen operating conditions of the combustors. These conditions include a pressure drop, Δp, of 3% across the height of the combustor, an outlet pressure of 1.0 atm, and an inlet temperature of 27 °C. These quantities were then used to determine the inlet air velocity.

Calculations were performed with the SSG RSTM and the standard κ–ε model using the quasi-second order upwind scheme in the KIVA code. The computed results were compared with the experimental data for the 60° co-rotating case. In addition, a 45° co-rotating was also investigated.

The experiments were conducted at the NASA Glenn Research Center. A square duct of quartz walls was used for the primary combustion zone for optical access. The sides of the square were 76.2 mm wide. A phase/Doppler particle analyzer was used for all velocity measurements. A two-component system using green (514.5 nm) and blue (488.0 nm) beams from an argon–ion laser operating at 1.5 W power output was used for the measurements. The transmitting optics utilized a 500 mm focal length lens combined with a 300 mm focal length collimating lens to yield a focused beam waist of 131 mm for the green and 124 mm for the blue lines. The fringe spacing was 6.788 mm for the green and 6.667 mm for the blue lines. The receiving optics were located 30° off-axis in the forward-scatter direction. Light was collected using a 500 mm focal-length f5.4 lens and then focused onto a 100 mm by 1 mm long slit. Further details of the instrument can be found in Ref. [12], and details of the experimental procedure can be found in Ref. [13].

2.2.1. 60° co-rotating swirlers case

Observations of the results on the X–Y planes in Figs. 10 and 11 show that the RSTM compares more closely to the experiments than does the κ–ε model. These plots display computed results at $Z = 5$ and 18 mm, while the experimental plots show the data measurements at the upper right corner of the same X–Y planes. A coordinate system is displayed on the figures to indicate the X and Y directions. The positive Z direction is directed from the swirler inlet to combustor outlet and is implied to be directed into the page.

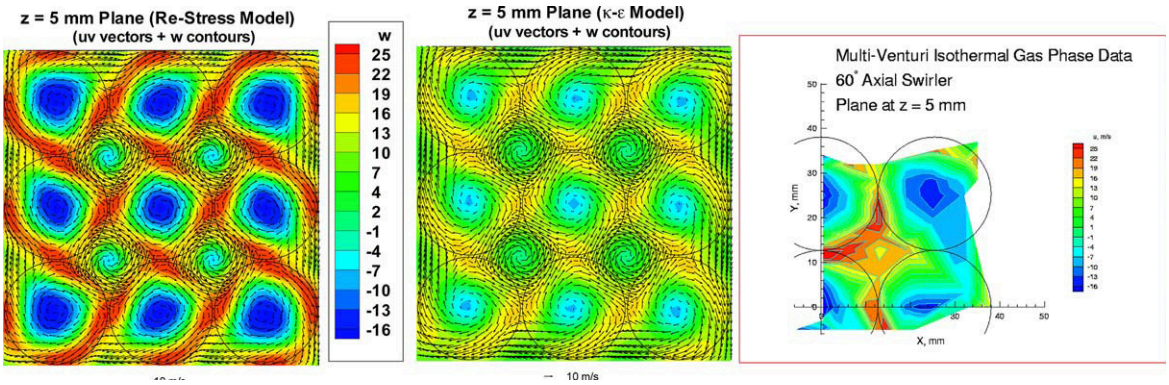

Fig. 10. Results for 60° swirler at $Z = 5$ mm cutting plane.

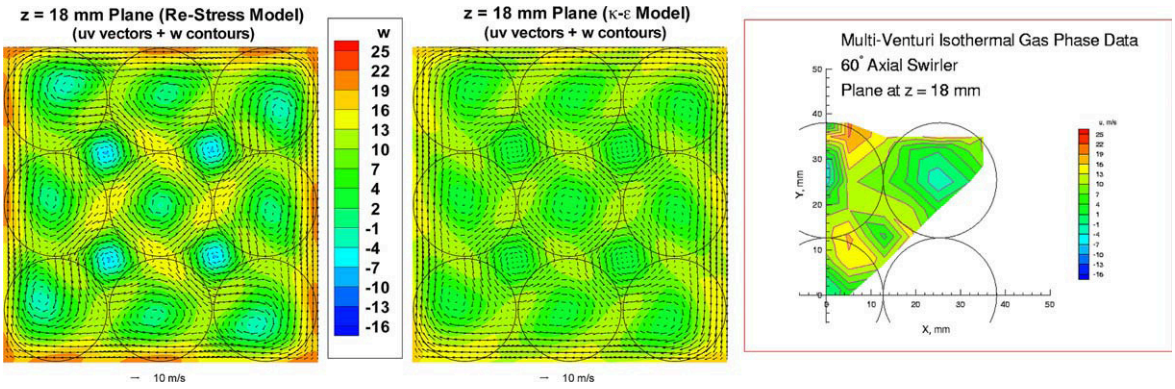

Fig. 11. Results for 60° swirler at $Z = 18$ mm cutting plane.

Fig. 10 paints a distinct picture that demonstrates the accuracy of the RSTM when comparing its result with the κ–ε and experimental plots. Between the two turbulence models, the magnitude of the velocities differ greatly, although the axial velocity (w) contour structures and the vector orientations display similarities. Comparison with the experimental data shows that the reversed flow at the center of the circles is better captured by the RSTM. The contour legend shows that the RSTM velocity levels vary over a greater range as seen in the experimental data plot.

At $Z = 18$ mm surface in Fig. 11, the RSTM result shows that the forward flow between swirlers and reversed velocity magnitude at the swirler centers are in good agreement with experiment. This shows that the RSTM can better predict the reversed flow associated with recirculations. It also shows its ability to resolve the effects of strong swirl as verified by the experimental data.

Additional observations can be made from Figs. 10 and 11. The four sub-regions enveloped by any four neighboring circles contain negative axial velocities (i.e., reversed flow) in the RSTM results, whereas the κ–ε plots present little (Fig. 10b) and no (Fig. 11b) reversed flow in these regions. Furthermore, these four sub-areas contain swirls in the counter-clockwise (ccw) direction, opposite to the primary flow direction from the nine swirlers. This is due to the opposing velocities surrounding the central circle, where the shear force in one direction impedes and steers away the shear force in the other, creating the four counter-clockwise swirls.

The contrast between the two models can be further displayed by viewing the velocity on the X–Z planes, such as along the $Y = 0.0$ mm cutting plane shown in Fig. 12. Reversed flow is much stronger below the swirlers with the RSTM. For example, the RSTM reversed flow reaches up to the venturi while the κ–ε result falls far short. Concurrently, the forward-flow regions predicted by the RSTM are also stronger. Since much of the cross section of the combustor has a reversed mass flux, the forward mass flux regions must be stronger to satisfy overall mass conservation.

The κ–ε model results appear more diffusive than those of the RSTM. This is due to the overestimated eddy viscosity which is a known characteristic of the standard κ–ε model. This set of results also indicates that without ad hoc modification, the κ–ε model is simply unable to cap-

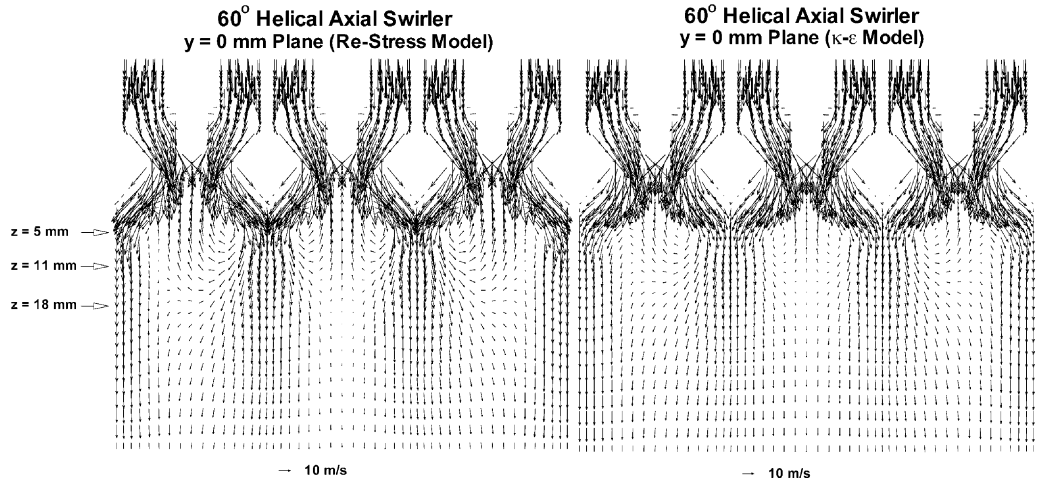

Fig. 12. Velocity vectors on $Y = 0.0$ mm cutting plane for 60° swirler.

ture the essence of flow recirculation from locally large axial pressure gradients created by the high degree of swirl [14]. As air exits from a swirler into the combustor, its swirling motion creates strong pressure gradients in the radial direction, a phenomenon similar to a free swirling jet being ejected from a nozzle. As the flow carries itself further downstream, an adverse pressure gradient builds up within the boundary of the air stream, causing the flow to reverse its axial direction and hence, a recirculation zone is created downstream of each swirler.

In short, with the RSTM whose Re-stress components are each computed with its own transport equation, the swirling and complex flow field can be resolved to an extent agreeable to the experiment. It can, therefore, be concluded that it is a valid model for the additional result comparisons discussed below.

2.2.2. 45° swirlers case study

The results obtained with the 45° swirler primarily display the significant differences between swirlers. The magnitude of the inlet velocity is the same as the 60° swirler case. As Figs. 13 and 14 indicate, there is no reversed flow at the center of the circles. Since the swirler diverts the upstream air at a smaller angle, a strong and solid forward-flow jet enters the combustor and does not permit recirculation as did the more conical jet from the 60° swirlers. Due to the lower degree of swirl, both turbulence models produce results almost identical to each other; however, weak recirculation regions are captured by the RSTM. Since the 45° swirler produces such weak swirl flow, these results show that both RSTM and κ–ε models can predict the flow field equally well.

The velocity profiles in Fig. 14 suggest that the atomization, vaporization, and mixing processes would occur less effectively with the 45° swirler. Fuel and air are injected directly downward into the primary zone, reducing the time for the three processes. Fuel–air jets around the perimeter are directed toward the wall and could lead to fuel droplet impingement on the walls. The lack of recirculation could reduce the amount of shear that aids in fuel atomization, and it could also reduce the degree of mixing that aids in uniform lean combustion.

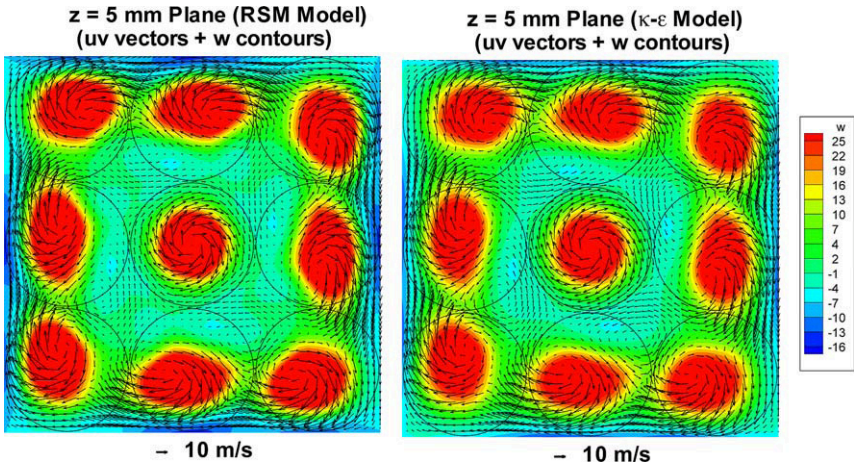

Fig. 13. Results for 45° swirler at $Z = 5$ mm cutting plane.

2.3. DISC engine

The DISC engine chamber whose 2D computational domain at -60° ATDC is displayed in Fig. 15. The chamber has a bore of 9.843 cm and a stroke of 9.55 cm. A chamfered bowl is located in the piston, and its cavity depth is 3.3 cm. The piston is located at -90° ATDC when the calculation starts. At this time, the fluid inside the cylinder has the composition of pure stagnant air at 400 K with a Bessel function swirl profile.

During the compression stroke, 11.6 mg of liquid gasoline in the form of a hollow cone spray is injected into the cylinder from an injector with a single half sine wave pulse, located close to the cylinder head axis. The injection begins at -52° ATDC and has a duration of 12.672°. Fig. 16 shows the κ–ε and SSG RSTM flow and temperature field results at -30° ATDC, shortly before ignition.

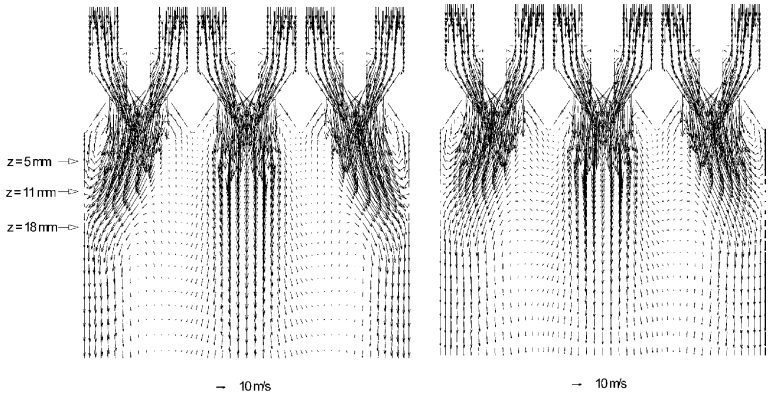

Fig. 14. Velocity vectors on $Y = 0.0$ mm cutting plane for 45° swirler.

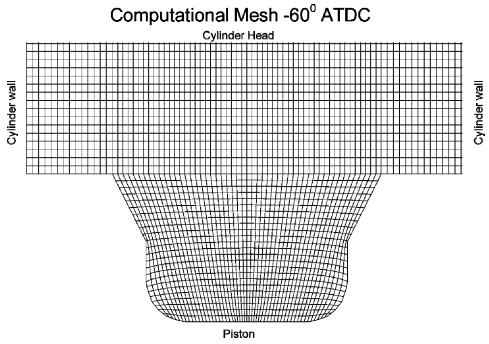

Fig. 15. DISC computational mesh.

The fuel–air mixture is subsequently spark-ignited at -27° ATDC. Drastic differences between RSTM and κ–ε model results can be observed from the figures. The magnitude of the eddy viscosity is overpredicted by the κ–ε model, which is expected since the model typically overpredicts μ_t. This can be seen in Fig. 17 for the effective viscosity. Because of the smaller eddy viscosity, the SSG RSTM results tend to show more distinct and localized profiles of temperature and effective viscosity. For example, the cooler region corresponding to the fuel spray at -30° ATDC is smaller and less diffuse for the RSTM model. In addition, the RSTM is able to perceive the spray in the effective viscosity contour plot. Distinctive profiles also exist at later angles as in Fig. 18, which focuses only on the bowl region. Here, the high temperature combustion gases are confined near the center of the bowl while several squish-induced circulation regions dominate the RSTM velocity profile. Highly diffusive variations are seen from the κ–ε results while only a defined structure appears from the RSTM. As shown, the anisotropic nature of the flow field is resolved only by the RSTM.

2.4. LPP combustor

The SSG RSTM was also applied to propane–air combustion in a lean, premixed, prevaporized (LPP) flame tube [15]. A study has been recently performed by Kundu et al. [16] with the κ–ε model and with a reduced reaction mechanism (23 kinetic reactions with 16 species) to

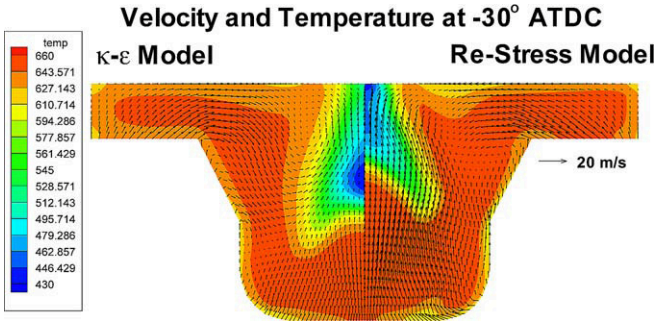

Fig. 16. Velocity vector and temperature at -30° ATDC.

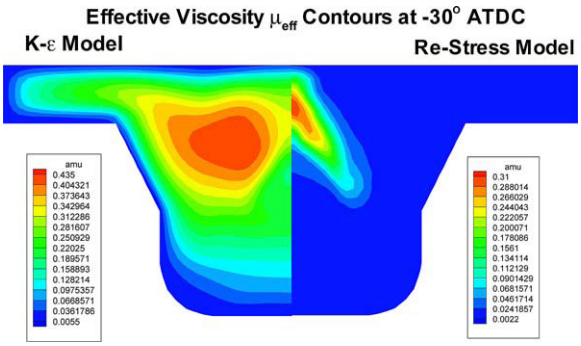

Fig. 17. Effective viscosity at -30° ATDC.

simulate the combustion and to evaluate NO_x emissions. The computational region displayed in Fig. 19 is 43 cm long and 10.2 cm in diameter. It includes the combustion zone, the flame holder, and a 10 cm length of the prevaporization/premixing zone. To reduce the domain into an axisymmetric model, the holes of the actual flame holder were approximated by several concentric rings. Therefore, only 4434 cells were required for a 2D radial mesh. An inlet velocity of 2500 cm/s and temperature of 800 K were specified in addition to an equivalence ratio of 0.8.

The results show differences between the RSTM and κ–ε models in terms of the velocity profile and NO_x emission index. Fig. 20 illustrates the computed velocity vectors for both models. It is apparent that the solution with the SSG model produces a large circulation zone on the wall-side of the flame tube that is not produced by the κ–ε model. In fact, the κ–ε model produces a velocity field that does not show any significant variation over the diameter of the flame tube, irrespective of the varying slot area and the much larger slot adjacent to the wall. The RSTM produces a velocity field that appears realistically descriptive of the fluid dynamics. This cannot be explicitly verified as there is no detailed experimental data of the velocity field for this particular case.

There are, however, experimental data of NO concentrations for this case. These data are given in the contour plots at the bottom of Fig. 21 and represents the measured EI

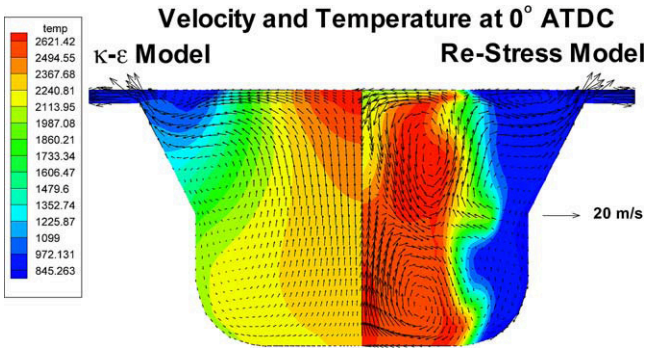

Fig. 18. Velocity vector and temperature at 0° ATDC.

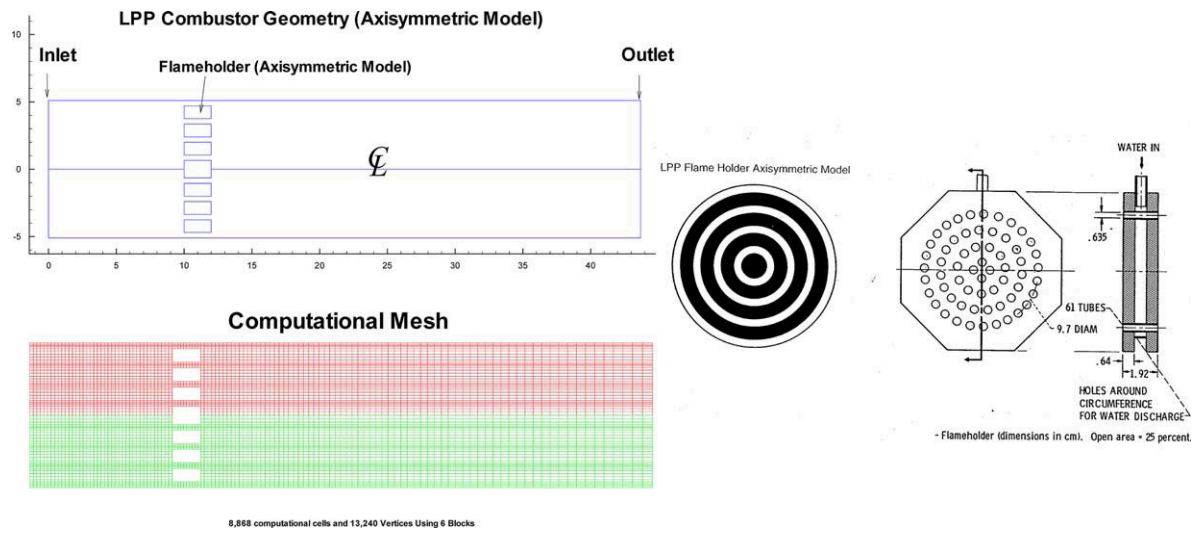

Fig. 19. LPP combustor computational model, mesh, and flame holder.

(g of NO_x/kg of fuel) along the centerline of the flame tube. In general, the levels of NO produced with the RSTM are closer to experimental values than those with the κ–ε model.

2.5. Four-valve DOHC engine

The last example shows the calculation of a four-valve DOHC engine using the standard κ–ε model in the KIVA code and the LRR RSTM without the wall-reflection term. The engine under consideration is 1200 c.c. with four cylinders and group port injection. Each cylinder has two intake and two exhaust valves and are canted at $\pm 10^{\circ}$. The engine has a compression ratio of 9.5, a 7.45 cm cylinder diameter (bore), 6.87 cm stroke, 11.27 cm connecting rod length, and operates at 1500 rpm. Fig. 22 shows the geometry and computational mesh of the DOHC engine. The valve lift history is given in Fig. 23.

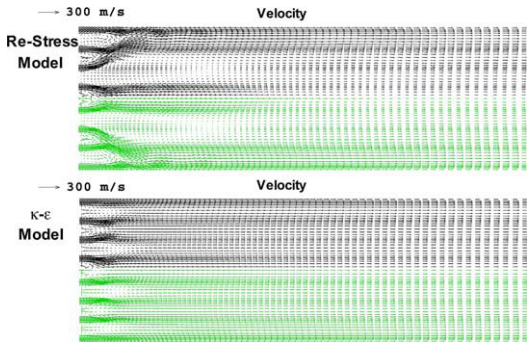

Fig. 20. Velocity vector.

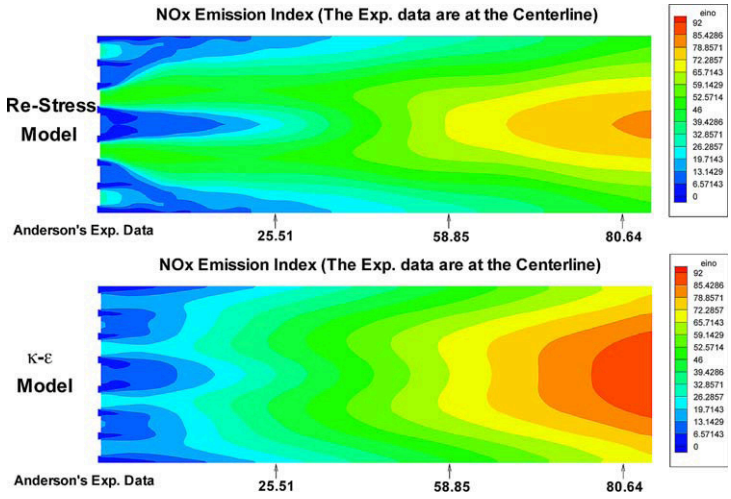

Fig. 21. NO_x emission index.

Fig. 24 shows the velocity vectors at different crank angles during intake and exhaust strokes. At the beginning of the intake, high-velocity air is drawn in through the intake valve and produces vortices below it, Fig. 24a. Both models show similar flow patterns at this crank angle (CA). At CA = 120°, just past the maximum lift (see Fig. 23), visible flow differences can be seen in Fig. 24b. Two vortices, one underneath the intake valve and the other near the bottom of the piston surface, are clearly shown in the LRR model prediction. Toward the end of the intake process, at CA = 180° (Fig. 24c), the vortex structures predicted by these two models are quite different, although the general flow patterns are somewhat similar. Hascher et al. [17] have

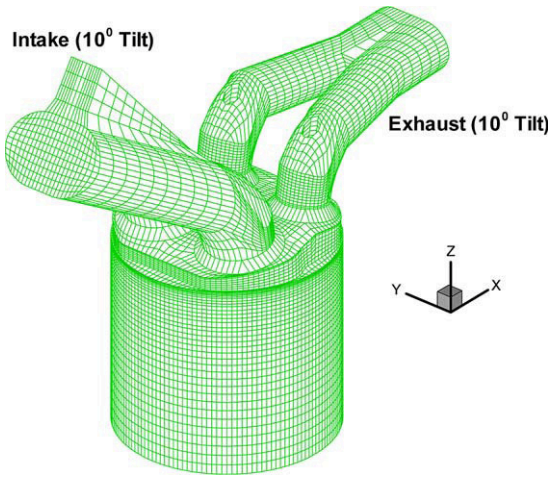

Fig. 22. Four-valve DOHC computational model.

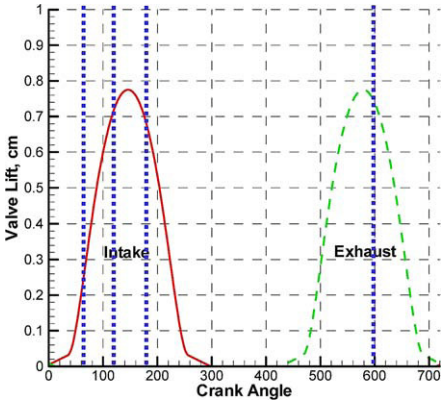

Fig. 23. Valve lift history.

also made similar observation when the experimental results were compared with the κ–ε model predictions using the Star-CD code. To gain a better understanding of the flow structure at this particular crank angle, Fig. 25 shows the 3D color-coded velocity vectors for both models. It can be seen that, due to the canted valves and the piston motion, the LRR model predicts stronger swirl flow. Near the peak of the exhaust stroke at CA = 600°, Fig. 24d, both models predict similar flow pattern, since relatively low level of turbulence exists in the flow field.

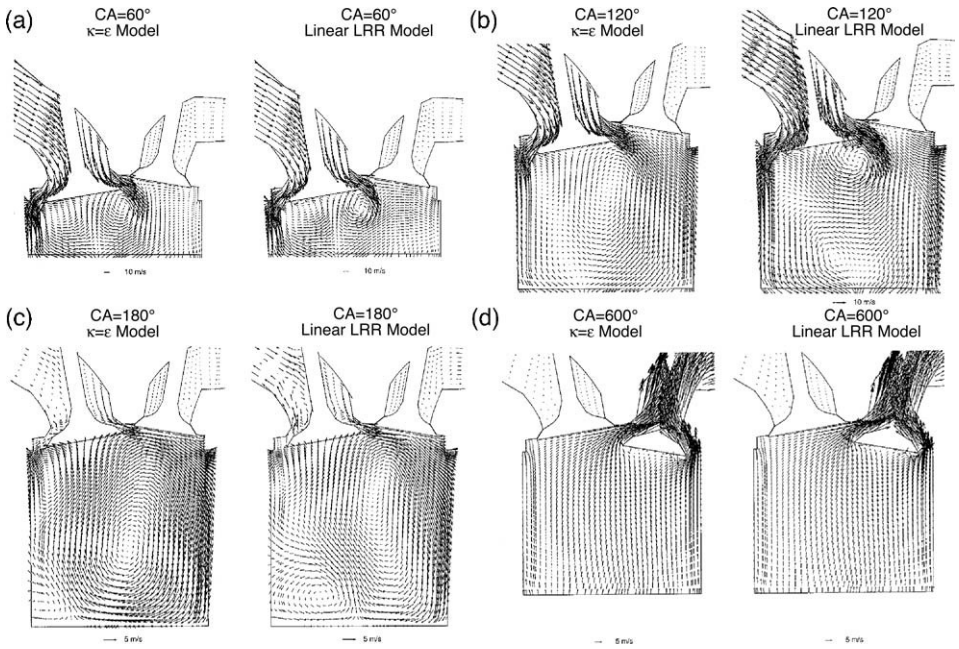

Fig. 24. Velocity vector at CA = 60°, 120°, 180°, and 600°.

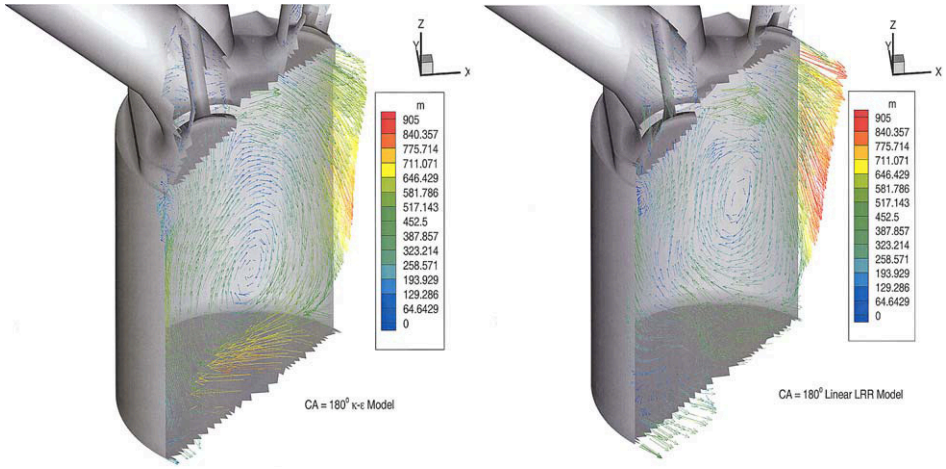

Fig. 25. 3D velocity vector at CA = 180°.

3. Conclusion

Two RSTMs were implemented within the KIVA code. Five application cases were studied to ascertain the performance of the RSTM by comparing the results with the κ–ε model predictions and the LDV measurements. Incorporated into the structure of the KIVA code, the RSTM was shown to successfully reproduce the mean flow features and second moments for a range of standard turbulent flow test cases, which include planar and axisymmetric flows. This provides confidence in applying the RSTM to engine type configurations. In these cases, the RSTM produces velocity and eddy viscosity fields that differ from the κ–ε model. Comparisons with the available, though limited, experiments, show that the RSTM results are more realistic. Unlike the κ–ε model, the RSTM is able to capture most recirculation structures, including those arising from the turbulent-stress anisotropy. In the studies of two LDI combustor cases, it further reveals that, for high degree swirl flows, the RSTM outperforms the κ–ε model. Further validation of the RSTM will be obtained in the future when compared with additional experimental measurements.

Acknowledgements

The authors would like to thank NASA Glenn Research Center for their financial assistance under NASA Grant Contract #NAG3-2088. The lead author would also like to thank the Delft University of Technology, The Netherlands, for providing him sabbatical leave support during the initial stage of this study.

References

[1] Lefebvre AH. Gas turbine combustion. USA: Hemisphere Publishing Corporation; 1983.

[2] Hanjalic K. Second-moment turbulence closures for CFD: needs and prospects. Int J Comp Fluid Dyn 1999;12:67–97.
[3] Launder BE, Reece GJ, Rodi W. Progress in the development of Reynolds-stress turbulence closure. J Fluid Mech 1975;68:537–66.
[4] Speziale CG, Sarkar S, Gatski TB. Modeling the pressure–strain correlation of turbulence: an invariant dynamical systems approach. J Fluid Mech 1991;227:245–72.
[5] Amsden AA. KIVA-3V, release 2: improvements to KIVA-3V, report No. LA-UR-99-915. Los Alamos (NM): Los Alamos National Lab.; 2000.
[6] Yang SL, Peschke BD, Hanjalic K. Second-moment closure model for IC engine flow simulation using KIVA code. ASME, J Eng Gas Turbines Power 2000;122:357–65.
[7] Iannetti A, Tacina R, Jeng S-M, Cai J. Toward accurate prediction of turbulent, three-dimensional, recirculation flows with the NCC. 39th AIAA Aerospace Sciences Meeting and Exhibit, Reno, NV, USA, January 8–11, 2001, AIAA-2001-0809.
[8] Liu N-S, Quealy A. NCC—a multi-disciplinary design/analysis tool for combustion systems. NASA 1998 Computational Aerosciences Workshop, August. 1998.
[9] Shih T-H, Chen K-H, Liu N-S, Lumley JL. Modeling of turbulent swirling flows, report No. NASA-TM-113112; 1998.
[10] Cai J, Jeng S-M, Tacina R. Multi-swirler aerodynamics: experimental measurements. 37th AIAA/ASME/SAE/ASEE Joing Propulsion Conference and Exhibit, Salt Lake City, UT, USA, July 8–11, 2001, p. 2001–3574.
[11] Teo CY, Siow YK, Yang SL. Flow filed study of LDI combustor with discrete jet swirlers using Re-stress model. 37th AIAA/ASME/SAE/ASEE Joing Propulsion Conference and Exhibit, Salt Lake City, UT, USA, July 8–11, 2001, p. 2001–3424.
[12] Bachalo WD, Houser MJ. Phase/doppler spray analyzer for simultaneous measurements of drop size and velocity distributions. Optical Eng 1984;23(5):583–90.
[13] Bulzan DL. Structure of a swirl-stabilized combusting spray. J Propul Power 1995;11(6):1093–102.
[14] Gupta AK, Lilley DG, Syred N. Swirl flows. Tunbridge Wells (England): Abacus Press; 1984.
[15] Anderson DA. Effects of equivalence ratio and dwell time on exhaust emissions from an experimental premixing prevaporizing burner, report No. NASA TMX-71592; 1975.
[16] Kundu KP, Penko PF, Yang SL. Reduced reaction mechanisms for numerical calculations in combustion of hydrocarbon fuels. 36th AIAA Aerospace Sciences Meeting and Exhibit, Reno, NV, USA, January 12–15, 1998, p. 98–803.
[17] Hascher HG, Schock HJ, Avanessian O, Novak J. A comparison of modeled and measured 3-D in-cylinder charge motion throughout the displacement of a four-valve SI engine. SAE-2000-01-2799, 2000.